

# Unraveling the Catalytic Graphitization Mechanism of Ni–P Electroless Plated Cokes via In Situ Analytical Approaches

Go Bong Choi, Jeong-Rae Ahn, Jungpil Kim, Tae Hoon Seo,\* and Sang Won Lee\*

Cite This: *ACS Omega* 2024, 9, 6741–6748

Read Online

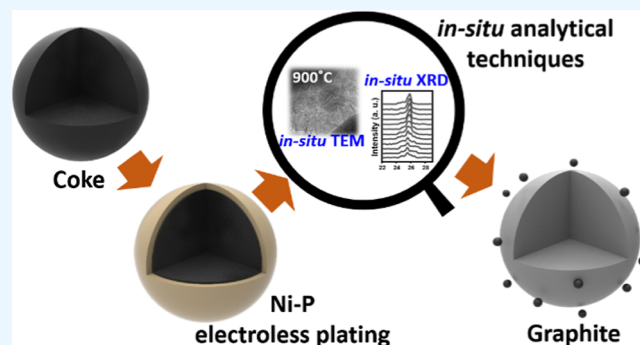
ACCESS |

Metrics &amp; More

Article Recommendations

Supporting Information

**ABSTRACT:** We elucidate the catalytic graphitization mechanism using in situ analytical approaches. Catalytic graphitization is achieved through a Ni–P electroless plating process at a relatively low temperature of 1600 °C, which allows for a high crystallinity of coke. We also employ an ultrasonic treatment during the Ni–P electroless plating stage to effectively form metal layers on the surface. The impact of the ultrasonic treatment on the Ni–P electroless plating is confirmed by field emission scanning electron microscopy images of the cross-section and an elemental composition analysis using energy dispersive X-ray spectroscopy mapping. Structural analysis of the graphitized cokes via X-ray diffraction (XRD) and Raman spectroscopy shows that Ni–P electroless plating significantly accelerates the graphitization process. Furthermore, we illuminate the graphitization behavior through in situ transmission electron microscopy and XRD analysis. Nickel layers on the coke surface facilitate graphite formation by encouraging the dissolution and precipitation of amorphous carbons, thus resulting in efficient graphitization at a relatively low temperature.



## 1. INTRODUCTION

Carbon materials are being extensively researched for their potential as electrode materials in next-generation storage devices due to their unique physical and chemical properties.<sup>1–4</sup> These electrode materials are required to have exceptional electrical conductivity and thermal/chemical stability. Among the various electrode materials, graphite notably offers high electrical conductivity and thermal stability.<sup>5,6</sup> However, the manufacture of artificial graphite presents challenges due to the extremely high temperatures exceeding 2500 °C and lengthy processing times it necessitates, thereby escalating costs and compromising productivity.<sup>7–9</sup> Moreover, achieving perfectly graphitized structures in amorphous carbon materials can prove arduous owing to inadequate heat transfer in the carbon network during high-temperature thermal treatment.<sup>10</sup> To overcome these problems, several techniques have been proposed to accelerate graphitization, such as external pressure or internal stress on the carbon materials.<sup>11–13</sup> Under high external pressure, the chemical potential of glassy carbon increases, rendering the transformation to graphite thermodynamically more favorable. Additionally, a phase diagram serves as an intuitive visual tool to delineate the stability domains of both glassy carbon and graphite across a spectrum of temperature and pressure conditions (Figure 1).<sup>14–16</sup> Contrastingly, stress graphitization relies on mechanical stress, such as compression, shear, or bending. The stress induces the carbon atoms to reorganize into a more ordered structure, thus facilitating the

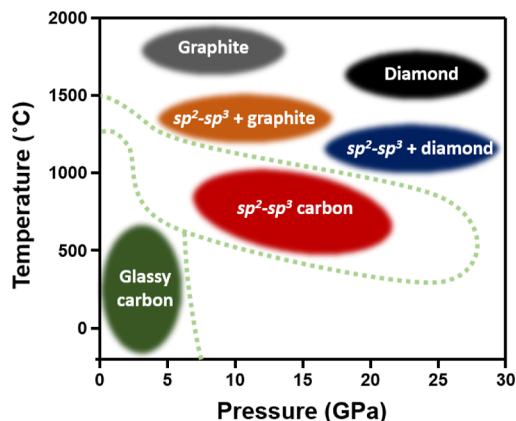


**Figure 1.** Phase diagram for glassy and graphitic carbons, depicting the pressure–temperature regions.

creation of a graphite structure.<sup>17,18</sup> However, the impact of pressure is limited by the distance from the surface of the

Received: October 15, 2023

Revised: January 8, 2024

Accepted: January 12, 2024

Published: January 31, 2024



carbon precursors, so stress graphitization mainly occurs at the interface of the carbon precursors.<sup>19,20</sup>

Catalytic graphitization is a transformative procedure that involves physical and chemical changes using transition metals as catalysts.<sup>21,22</sup> Metal catalysts such as nickel (Ni), cobalt (Co), and iron (Fe) decrease the activation energy required to transform amorphous carbon into a high-crystalline structure, leading to graphitization reactions at lower temperatures. Generally, two primary mechanisms have been suggested for catalytic graphitization methods:<sup>23–25</sup> (1) the dissolution of carbon into catalysts followed by its excretion as graphite material; and (2) the formation and subsequent decomposition of carbide intermediates. However, these inferred mechanisms of catalytic graphitization have been limited by the constraints of analysis, thereby necessitating further comprehensive studies employing more precise analytical methods. Notably, Ni and/or Ni-based alloys are recognized as one of the most effective catalysts for the graphitization of amorphous carbon materials.<sup>26–28</sup> The application of Ni particles onto the surface of carbon precursors was meticulously executed via an electroless plating technique. Contrary to electroplating, electroless plating is a method of metal plating that involves a selective reduction reaction of metal ions on the surface. Since the electroless plating method is free from electric force, it can be used to achieve uniform plating even on complex shapes and can also be used to plate insulators.<sup>29,30</sup> Phosphorus concentration in nickel electroless plating can have an important effect on solderability, coating uniformity, and smoothness. Controlling the deposition rate by phosphorus introduction allows for a more even and consistent distribution of the nickel layer across complex geometries and surfaces.<sup>31,32</sup> Ni–P alloys have an amorphous or microcrystalline structure, especially when the phosphorus content is high. The amorphous nature contributes to a more uniform and homogeneous coating, which is less likely to have defects like pores or cracks that can initiate corrosion.<sup>33</sup> In addition, the electroless plating process allows for a controlled and uniform deposition of the Ni–P alloy, ensuring consistent coverage and thickness.<sup>34,35</sup> This uniformity is essential for providing consistent corrosion resistance across the entire coated surface.

In this study, catalytic graphitization was carried out by using Ni–P electroless plating to ensure stability and corrosion resistance during in situ analysis. Coke samples were initially coated with Ni–P through an ultrasonic-assisted electroless plating method and then thermally treated at 1600 °C. The surface morphology and cross-section of the samples were investigated by scanning electron microscopy (SEM) and energy-dispersive X-ray spectroscopy (EDS). We evaluated the changes in crystallinity before and after graphitization by X-ray diffraction (XRD) and Raman spectroscopy. Finally, we delved into the impact of Ni–P electroless plating on the graphitization process by deploying in situ transmission electron microscopy (TEM) and XRD techniques.

## 2. EXPERIMENTAL SECTION

**2.1. Materials.** The Ni–P electroless plating solution (ENF, Young-In Plachem Co., Korea) used in the experiment was based on nickel sulfate (Table 1). An electroless plating bath was composed of phosphorus (8%) and nickel (6 g/L). A commercial product was purchased and used for reproducibility. Petroleum-based coke (Anshan Iron and Steel Group Corporation, China) was sieved to make the size uniform between 200 and 250  $\mu\text{m}$ . Tin chloride ( $\text{SnCl}_2$ ), hydrochloric

**Table 1. Bath Condition of Electroless Ni–P Plating**

electroless Ni–P plating bath	values
phosphorus (P)	8%
concentration (Ni)	6 g/L
precipitation rate	15–20 $\mu\text{m}/\text{h}$
pH	4.6

acid (HCl), nitric acid ( $\text{HNO}_3$ ), and palladium chloride ( $\text{PdCl}_2$ ) were obtained from DEAJUNG Chem., Korea.

**2.2. Catalytic Graphitization via Electroless Ni–P Plating.** Figure 2 shows a schematic of the electroless plating process. To remove impurities on the surface of coke, 10 g of coke was added to 100 mL of 5 M  $\text{HNO}_3$  aqueous solution and stirred for 30 min. After stirring, the samples were neutralized by washing several times with distilled water. The purified samples were placed in a 0.0014 M  $\text{PdCl}_2$  aqueous solution, and the mixture was stirred for 30 min. The coke samples were washed with distilled water and dried in a vacuum oven at 80 °C for 1 h. After a catalytic impregnation, the coke samples of 2 g were added into the plating solution of 300 mL at an optimum plating temperature of 90 °C. The ultrasonic treatment was additionally introduced to improve the plating layer uniformity and accelerate the plating speed. The Ni–P electroless-plated cokes were thermally treated at 1600 °C for graphitization. A tube-type heating furnace was used with a heating rate of 1 °C/min under Ar gas flow at 200  $\text{cm}^3/\text{min}$ . The coke samples were plated with Ni–P solution using only an immersing treatment and an ultrasonic treatment after the immersing process. Four plating samples were synthesized: a sample with 15 min of immersing treatment (Ni–I15) and three samples with 5 min of immersing treatment followed by 3 min. (Ni–I5–S3), 5 min. (Ni–I5–S5), and 10 min (Ni–I5–S10) of ultrasonic treatment. Moreover, thermally treated Ni–P electroless plated coke samples at 1600 °C were assigned as H16–Ni–I15, H16–Ni–I5–S3, H16–Ni–I5–S5, and H16–Ni–I5–S10.

**2.3. Characterizations.** After the Ni–P electroless plating, the surface of the coke samples was analyzed using SEM (AIS2000C, Seron Tech Inc., Korea). To analyze the structure and thickness of the plating layer, the cross-section of cokes was verified using field emission scanning electron microscopy (FE-SEM, JSM-7100F, Jeol Ltd., Japan) and energy-dispersive X-ray spectroscopy (EDS, X-act, Ultim Max Oxford Instruments Plc., United Kingdom). XRD (MiniFlex, Rigaku co., Japan) was used with Cu  $K\alpha$  radiation ( $\lambda = 1.5406 \text{ \AA}$ ), and the measurement range was 3 to 80° at a rate of 4°/min. In order to defect of accelerate graphitized cokes, Raman spectroscopy (RAMANforce, Nanophoton, Japan) was done with a spectrometer equipped with a CCD detector. The laser wavelength used to excite the samples was 532 nm. The in situ TEM (Cs-Corrected STEM, ARM-200F, Jeol Ltd., Japan) analysis is conducted in the temperature range of 25 to 900 °C at a heating rate of 1 °C/s. The in situ XRD (Malvern Panalytical Ltd., United Kingdom) analysis was performed to confirm the coke change in crystallinity heat-treated at a temperature up to 1200 °C. During the in situ XRD analysis, an argon gas was flowed to maintain an inert atmosphere in the range of 10–80°. It was measured over 30 min, and each time, the temperature rose by 100 °C in the range of 600 to 1200 °C. After reaching 1200 °C, we carried out the thermal treatment at 1200 °C for 4 h.

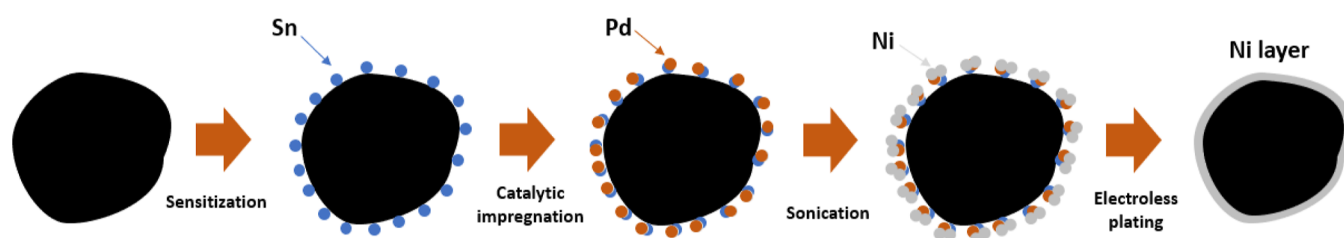


**Figure 2.** Schematic diagram of electroless plating for the introduction of metal catalysts into coke. Sensitization, activation (introduction of palladium catalyst), and plating proceed in order, and ultrasonic treatment was added to ensure plating uniformity.

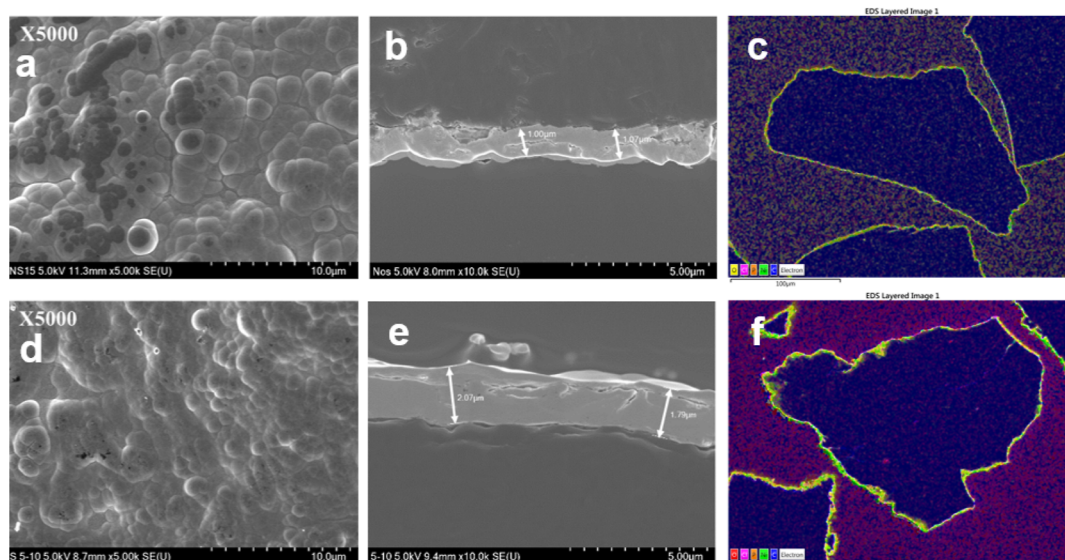


**Figure 3.** FE-SEM images of surface for (a) Ni-I15 and (d) Ni-I5-S10 and cross-section for (b) Ni-I15 and (e) Ni-I5-S10 and elemental composition analysis of (c) Ni-I15 and (f) Ni-I5-S10 using energy dispersive X-ray spectroscopy (EDS) mapping (color code of the map: carbon in blue, oxygen in yellow, chloride in pink, and nickel in green).

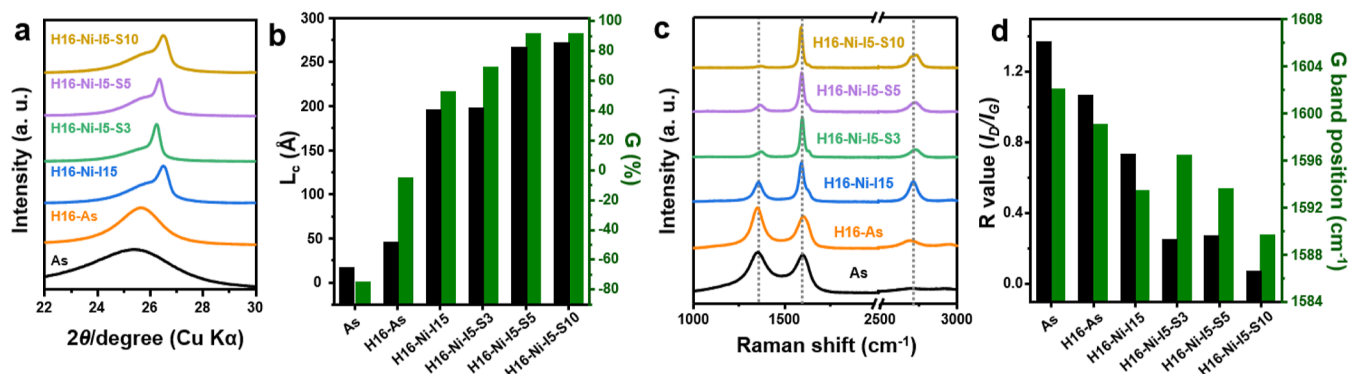


**Figure 4.** (a) XRD patterns and (c) Raman spectra of thermally treated Ni-P-plated cokes at 1600 °C, (b) crystalline size and the degree of graphitization from XRD data, and (d)  $R$  value and the position of the G band from the Raman spectra of the various coke samples.

### 3. RESULTS AND DISCUSSION

The Ni-P electroless plating process was carried out in a uniform manner, including several stages such as sensitization and catalytic impregnation (Figure 2). The Ni-P electroless plating process employs the utilization of tin (Sn) and palladium (Pd), with each element playing distinct and specific roles. In the pretreatment phase of plating, it is typical to employ two elements, mainly Sn and Pd. Specifically, Sn serves the purpose of activating and stabilizing the coating layer, while Pd functions as a catalytic activation layer.<sup>36–38</sup> Accordingly, both tin (Sn) and palladium (Pd) play essential roles in the

Ni-P electroless plating process, having a significant influence on the quality and uniformity of the coating (Figure S1). Figure 3 shows the effect of ultrasonication pretreatment during Ni-P electroless plating by drawing a comparison between samples treated with and without ultrasonication. In order to address the problem of exfoliation arising during the electroless plating process, an immersion step is introduced before the ultrasonication treatment. Consequently, we established two electroless plating conditions: immersion only (Ni-I15) and immersing-ultrasonication (Ni-I5-S10). FE-SEM images in Figures 3 and S2 depict the surface and

cross-sectional morphology of the cokes, both treated and untreated with ultrasonication. The surface of the coke without ultrasonication (Ni-I15) presents relatively large metal particles, whereas the coke with ultrasonication (Ni-I5-S10) exhibits a dense arrangement of smaller metal particles (refer to Table S1 and Figure 3a,d). We can infer that spherical Ni-P islands form near the plating nucleus and cluster together to form a single layer during the plating process. Additionally, the cross-sectional analysis of the ultrasonicated sample (Ni-I5-S10) reveals a plated layer approximately 2  $\mu\text{m}$  thick, nearly twice the thickness of the untreated coke (Ni-I15) (Figure 3b,e). EDS mapping images of the cross-section also indicate a prominent and thick nickel source at the surface of the ultrasonicated coke sample (Figure 3c,f). A successful Ni-P plating was further confirmed through XPS and  $\text{N}_2$  adsorption/desorption analysis (Figures S3 and S4), with their respective results summarized in Table S2. As the Ni-P plating progressed, the contents of both Ni and P increased. The presence of  $\text{Ni}^{\delta+}$  species and reduced phosphorus in the Ni 2p and P 2p spectra confirms the formation of a Ni-P alloy compound.<sup>39,40</sup> While the overall pore structure remains nonporous, it is noted that the formation of the Ni-P layer led to a reduction in both surface area and pore volume. These findings suggest that ultrasonic treatment can enhance not only the homogeneity but also the formation rate of the plating layer.

Figure 4 presents the XRD patterns and Raman spectra of pristine and Ni-P electroless plating cokes after thermal treatment at 1600 °C. After heat treatment, the amount of metal remaining on the surface significantly decreased, with 93.73% C, 0.55% P, and 5.72% Ni detected. The XRD patterns of the coke samples reveal a peak near 26°, corresponding to the (002) graphite peak (Figure 4a). The structural changes after various post-treatments were investigated based on the values of interlayer spacing ( $d_{002}$ ), crystallite size ( $L_c$ ), and degree of graphitization ( $G$ ) presented in Table 2. It is clear

**Table 2. Crystallographic Parameters Derived from XRD and Raman Spectroscopy for the Ni-P-Plated Coke Samples**

	$d_{002}$ <sup>a</sup> (Å)	$L_c$ <sup>b</sup> (Å)	$G$ (%) <sup>c</sup>	R-value ( $I_D/I_G$ ) <sup>d</sup>	G-band ( $\text{cm}^{-1}$ ) <sup>e</sup>
As <sup>f</sup>	3.505	15.6	−75.6	1.368	1602.0
H16-As	3.445	45.0	−5.81	1.063	1599.0
H16-Ni-I15	3.395	195	52.3	0.731	1593.4
H16-Ni-I5-S3	3.381	197	68.6	0.246	1596.4
H16-Ni-I5-S5	3.362	266	90.7	0.267	1593.5
H16-Ni-I5-S10	3.362	271	90.7	0.069	1589.6

<sup>a</sup> $d_{002}$  indicates interlayer spacing from the XRD patterns. <sup>b</sup> $L_c$  indicates crystallite size from XRD. <sup>c</sup> $G$  is the graphitization degree calculated from XRD. <sup>d</sup>R-value ( $I_D/I_G$ ) is the integrated intensity of the D band divided by the integrated intensity of the G band in Raman spectra. <sup>e</sup>G-band is the position of the highest peak in the G band, and. <sup>f</sup>As is as-prepared pristine coke sample.

that the 002 peak became upshifted and sharper when Ni-P electroless plating was applied prior to graphitization. For instance, the coke subjected to only thermal treatment exhibits a crystallite size of 15.6 Å (H16-As). In contrast, the Ni-P electroless plated cokes, prepared by immersing or immersing-ultrasonication, display larger crystallite sizes of 195 Å (H16-Ni-I15) and 271 Å (H16-Ni-I5-S10), respectively. These findings suggest that the incorporation of Ni-P electroless

plating significantly enhances the crystallinity of the resulting cokes during the graphitization process. Additionally, the degree of graphitization was calculated using the following formula:  $G = (3.440 - d_{002}) / (3.440 - 3.354) \times 100$ . In this equation,  $G$  represents the degree of graphitization (%), and the values 3.440 and 3.354 denote the interlayer spacing (Å) of turbostratic carbon and ideal graphite crystallite, respectively.<sup>41,42</sup> The coke thermally treated at 1600 °C has a low  $G$  value of −5.81%, which is even lower than that of turbostratic carbons due to the insufficient temperature for graphitization. However, the  $G$  value increases significantly, up to 90.7%, when Ni-P electroless plating is combined with the ultrasonication process (Table 2). In the context of the Ni-P electroless plating process, the coke treated by immersion (H16-Ni-I15) has a  $G$  value of 52.3%, which is considerably lower than the 90.7% value observed for the coke treated by immersion and ultrasonication (H16-Ni-I5-S10). Figure 4 illustrates the crystallite size and the degree of graphitization for graphitized coke samples under various conditions. It is noteworthy that the crystallinity parameters derived from the XRD data were improved with Ni-P electroless plating and ultrasonic treatment. Note that the homogeneous Ni-P electroless plating layer accelerates graphitization, resulting in an increase in the crystalline size and the degree of graphitization.

To further investigate the structural development induced by catalytic graphitization, we conducted Raman spectroscopy measurements of the coke samples. Carbon materials typically exhibit three main Raman peaks centered at 1350, 1580, and 2700  $\text{cm}^{-1}$ , corresponding to the D, G, and 2D bands. The D and G bands are associated with  $\text{sp}^2$ -bonded carbon atoms and defect-induced carbon structures, respectively.<sup>43,44</sup> Therefore, the  $R$  value ( $I_D/I_G$ , the integrated area of the D band divided by that of the G band) serves as a critical parameter for characterizing the crystallinity of the coke samples. The  $R$  value of coke samples heat-treated at 1600 °C decreased from 1.063 to 0.731 upon the introduction of Ni-P electroless plating via the immersing process and further declined to 0.069 when ultrasonic treatment was incorporated during the Ni-P electroless plating process (Figure 4c and Table 2). This considerable reduction in the  $R$  value demonstrates the significant impact of ultrasonication on enhancing the crystallinity and overall quality of the resulting graphitized coke. The 2D band, originating from overtone scattering of the D band, becomes more intense as stacking structures are enhanced through accelerated graphitization. Furthermore, a down-shift in the G band is observed, from 1602  $\text{cm}^{-1}$  (as-prepared coke) to 1590  $\text{cm}^{-1}$  (H16-Ni-I5-S10), indicating the transformation of imperfect hexagonal lattices into highly crystalline structures (Table 2).<sup>45,46</sup> Following graphitization at 1600 °C, all Ni-P-plated coke samples exhibit superior crystallinity compared to the untreated coke sample (Figure 4d). The combined results from Raman spectroscopy and XRD analysis clearly demonstrate that catalytic graphitization facilitated by Ni-P electroless plating effectively accelerates the graphitization process, thereby significantly enhancing the crystallinity of the resulting coke (Figure 4b,d).

To elucidate the mechanism of catalytic graphitization, we conducted in situ TEM analysis on Ni-P electroless plating cokes during thermal treatment up to 900 °C (Figure 5). We obtained a series of video images capturing the boundary between the coke's surface and Ni-P layers at 100 °C intervals. At the initial stage of 25 °C, amorphous carbon

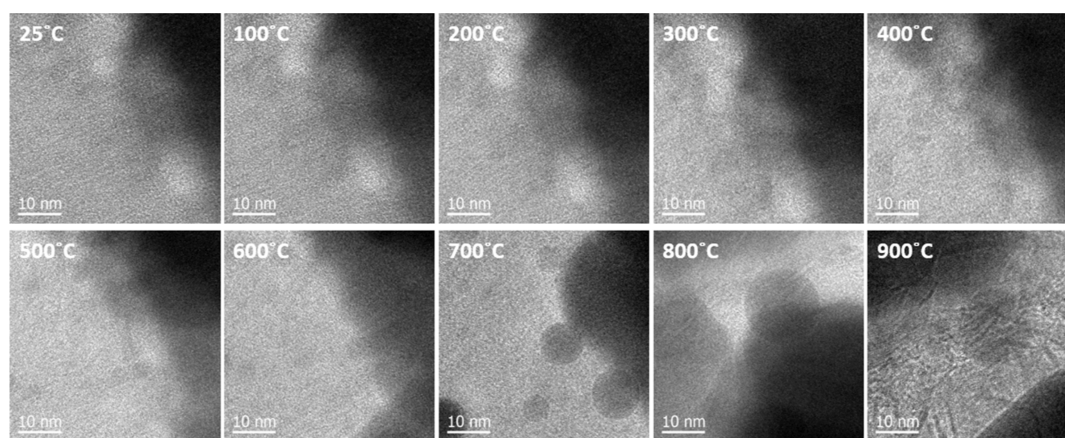


Figure 5. In situ TEM images of Ni–P-plated coke during thermal treatment up to 900 °C.

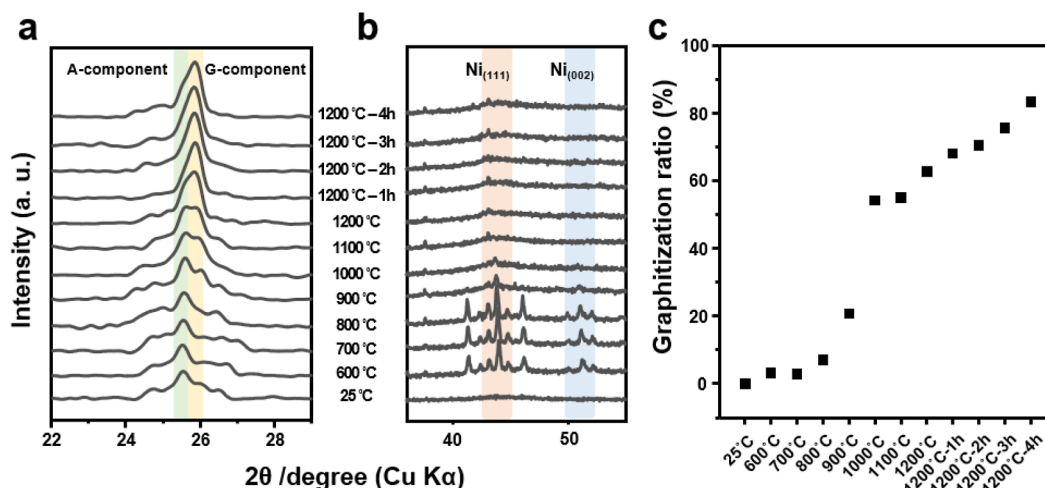
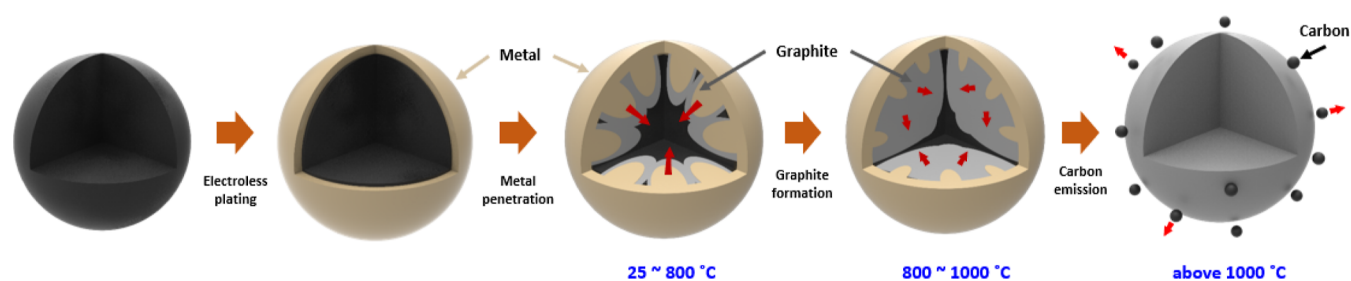


Figure 6. (a,b) In situ XRD patterns of Ni–P-plated coke in the range of 22–29° (a) and 35–45° (b,c) graphitization ratio at different temperatures.

structures with nongraphitized networks are observed. Minimal changes are detected from 25 to 400 °C, but at 500 and 600 °C, some indistinct metal particles originating from the decomposition of metal precursors become apparent. At 700 °C, nickel particles disperse and migrate into the amorphous carbon, which subsequently dissolves randomly into nickel at 800 and 900 °C. The interaction between nickel and carbon is facilitated by the dissolution of amorphous carbon, leading to the release of carbon in the form of graphitic carbon structures in the vicinity of the nickel particles. Consequently, the emergence of graphite structures is observed starting at 900 °C. These findings provide valuable insights into the intricate interplay between nickel and carbon during catalytic graphitization, highlighting the crucial role of Ni–P electroless plating in facilitating the formation of highly crystalline graphitized coke structures.

To further understand the catalytic graphitization mechanism observed in the in situ TEM images, we carried out in situ XRD analysis. Two main peaks were identified at approximately 25.5 and 26°, corresponding to the amorphous component (A-component) and graphitic component (G-component), respectively (Figure 6a).<sup>47</sup> The graphitization ratio was calculated by dividing the area of the G component by the total area of the peaks (Figure 6c). At room temperature, the Ni–P electroless-plated coke exhibits a

broad peak for the A-component at 25.5°, indicative of a predominantly amorphous carbon structure. During thermal treatment, the graphitization ratio increased progressively as the treatment temperature rose. The graphitization process can be divided into three distinct stages based on specific temperature ranges: (1) 25–800 °C, a slight increase in the graphitization ratio; (2) 800–1000 °C, a dramatic increase in the graphitization ratio; and (3) above 1000 °C, the formation of graphitized structures. The graphitization ratio exhibited a more pronounced increase with extended holding time during thermal treatment at 1200 °C. Consequently, the Ni–P-plated coke thermally treated at 1200 °C for 4 h achieved a graphitization ratio of 83.44%. Throughout thermal treatment up to 1200 °C, the Ni–P-plated coke samples display a negligible broad peak near 44.5°, corresponding to the (100) plane of the aromatic structure. However, sharp and strong peaks at 44.5 and 51° emerged within the temperature range of 600–800 °C (Figure 6b). This observation can be attributed to the decomposition of the nickel plating layer, which releases nickel nanoparticles and results in sharp peaks at 44.5 and 51°, corresponding to the (111) and (002) planes of nickel, respectively.<sup>48,49</sup> As the thermal treatment temperature rose beyond 800 °C, these nickel peaks diminished due to the infiltration of nickel nanoparticles into the interior of the amorphous carbon. In addition, the detailed XRD patterns for



**Figure 7.** Schematic illustration of the catalytic graphitization mechanism using electroless plating.

Ni–P-plated coke and thermally treated Ni–P-plated coke at 600 °C were obtained to verify the  $\text{Ni}_x\text{P}_y$  nanostructures, as shown in Figure S5. Based on the JCPDS card file data, it can be observed that the Ni–P-plated coke sample undergoes a transformation from nickel nanoparticles to hexagonal  $\text{Ni}_2\text{P}$  phase at a thermal treatment temperature in the range of 600–800 °C.<sup>50,51</sup> Further increasing the thermal treatment temperature to above 900 °C promotes graphitization, leading to the disappearance of the  $\text{Ni}_x\text{P}_y$  nanostructures. These behaviors highlight the vital role played by nickel nanoparticles in enhancing the crystallinity of carbon structures through their interaction with amorphous carbon during thermal treatment.

The in situ XRD results demonstrate a temperature-responsive graphitization mechanism that aligns with the observations gleaned from the in situ TEM studies. This is indicative of a carbon dissolution–precipitation mechanism, which is accelerated by Ni–P electroless plating, thus facilitating catalytic graphitization. A well-documented understanding in the field posits that nickel, unlike certain other metals, does not form a carbide phase.<sup>52,53</sup> Building on these analytical observations, the graphical representation in Figure 7 depicts the catalytic graphitization process that incorporates Ni–P electroless plating. Originating from the electroless plating, the nickel layer undergoes a decomposition process, leading to the formation of nickel nanoparticles. With a rising temperature, these nickel nanoparticles disperse and permeate the amorphous coke matrix. Once embedded within the coke, the nickel nanoparticles act as a catalyst in the creation of graphite structures, and the dissolved carbon precipitates out, morphing into graphite with a highly advanced crystalline structure. This in-depth analysis provides valuable insights into the mechanisms underpinning catalytic graphitization and emphasizes the crucial role played by nickel nanoparticles in enhancing the crystallinity of carbon materials.

#### 4. CONCLUSIONS

In this study, we elucidated the catalytic graphitization mechanism using in situ analytical techniques, including TEM and XRD. Investigations carried out using SEM and EDS revealed the presence of thick and uniform plating layers resulting from ultrasonic treatment. In the XRD and Raman spectra, the Ni–P electroless-plated sample with ultrasonic treatment exhibited a significant improvement in crystallinity following thermal treatment at 1600 °C, achieving a graphitization degree of 90.7% and an *R* value of 0.069. To uncover the mechanism behind catalytic graphitization using Ni–P electroless plating, we systematically performed in situ TEM and XRD analyses. The accelerated graphitization can be attributed to a carbon dissolution–precipitation mechanism. By in situ analytical techniques, we demonstrated that the graphitization process can be divided into three distinct stages

based on specific temperature ranges: (1) 25–800 °C, characterized by a slight increase in the graphitization ratio with a relatively flat gradient; (2) 800–1000 °C, marked by a dramatic increase in the graphitization ratio; and (3) above 1000 °C, in which graphitized structures begin to stabilize. Therefore, nickel nanoparticles facilitated the formation of graphite structures by expediting the dissolution and precipitation of amorphous carbons, thereby achieving efficient graphitization at a relatively low temperature of 1600 °C.

#### ■ ASSOCIATED CONTENT

##### SI Supporting Information

The Supporting Information is available free of charge at <https://pubs.acs.org/doi/10.1021/acsomega.3c07692>.

Detailed information of Ni–P-plated cokes; elemental content by EDS; SEM image for morphology;  $\text{N}_2$  adsorption/desorption isotherm; pore size distribution; Ni 2p and P 2p spectra for Ni–P-plated coke samples; structural information of pristine and Ni–P-plated cokes; EDS mapping images; XRD spectra of Ni–P-plated cokes before and after thermal treatment at 600 °C; and TEM images of Ni–P-plated cokes before and after catalytic graphitization (PDF)

#### ■ AUTHOR INFORMATION

##### Corresponding Authors

Tae Hoon Seo – Green Energy & Nano Technology R&D Group, KITECH, Gwangju 61012, Republic of Korea; Email: [thseo@kitech.re.kr](mailto:thseo@kitech.re.kr)

Sang Won Lee – Industrialization Division, Korea Carbon Industry Promotion Agency (KCARBON), Jeonju 54853, Republic of Korea; [orcid.org/0009-0003-1379-4639](https://orcid.org/0009-0003-1379-4639); Email: [swonlee00@kcarbon.or.kr](mailto:swonlee00@kcarbon.or.kr)

##### Authors

Go Bong Choi – Korea Advanced Institute of Science and Technology (KAIST), Daejeon 34141, Republic of Korea

Jeong-Rae Ahn – Industrialization Division, Korea Carbon Industry Promotion Agency (KCARBON), Jeonju 54853, Republic of Korea

Jungpil Kim – Carbon & Light Materials Application Research Group, Korea Institute of Industrial Technology (KITECH), Jeonju 54853, Republic of Korea; [orcid.org/0000-0003-3663-2774](https://orcid.org/0000-0003-3663-2774)

Complete contact information is available at: <https://pubs.acs.org/10.1021/acsomega.3c07692>

## Author Contributions

The manuscript was written through the contributions of all authors. All authors have given approval to the final version of the manuscript.

## Notes

The authors declare no competing financial interest.

## ACKNOWLEDGMENTS

S.W.L. acknowledges the financial support from the Technology Innovation Program (no. 20006777) funded by the Ministry of Trade, Industry & Energy (MOTIE) and the National Research Foundation of Korea (NRF) grant funded by the Korea government (MSIT) (2019R1A5A8080326). T.H.S. acknowledges the financial support from the Korea Institute of Industrial Technology under the Development of Core Technologies for Smart Mobility (KITECH JA-23-0011) and the Basic Science Research Program through the National Research Foundation of Korea (NRF), funded by the Ministry of Education, Science, and Technology (NRF-2022R1F1A1074422).

## REFERENCES

- (1) Bi, Z.; Kong, Q.; Cao, Y.; Sun, G.; Su, F.; Wei, X.; Li, X.; Ahmad, A.; Xie, L.; Chen, C. M. Biomass-derived porous carbon materials with different dimensions for supercapacitor electrodes: a review. *J. Mater. Chem. A* **2019**, *7*, 16028–16045.
- (2) Kumar, S.; Saeed, G.; Zhu, L.; Hui, K. N.; Kim, N. H.; Lee, J. H. 0D to 3D Carbon-Based Networks Combined with Pseudocapacitive Electrode Material for High Energy Density Supercapacitor. *Chem. Eng. J.* **2021**, *403*, 126352.
- (3) Zhang, L.; Zhao, X. S. Carbon-Based Materials as Supercapacitor Electrodes. *Chem. Soc. Rev.* **2009**, *38*, 2520–2531.
- (4) Liang, J.; Sun, Z. H.; Li, F.; Cheng, H. M. Carbon Materials for Li-S Batteries: Functional Evolution and Performance Improvement. *Energy Storage Mater.* **2016**, *2*, 76–106.
- (5) Wang, C.; Xia, K.; Wang, H.; Liang, X.; Yin, Z.; Zhang, Y. Advanced Carbon for Flexible and Wearable Electronics. *Adv. Mater.* **2019**, *31*, 1801072.
- (6) Wu, Z. S.; Ren, W.; Gao, L.; Zhao, J.; Chen, Z.; Liu, B.; Tang, D.; Yu, B.; Jiang, C.; Cheng, H. M. Synthesis of Graphene Sheets with High Electrical Conductivity and Good Thermal Stability by Hydrogen Arc Discharge Exfoliation. *ACS Nano* **2009**, *3* (2), 411–417.
- (7) Shi, M.; Tai, Z.; Li, N.; Zou, K.; Chen, Y.; Sun, J.; Liu, Y. Spherical Graphite Produced from Waste Semi-Coke with Enhanced Properties as an Anode Material for Li-Ion Batteries. *Sustainable Energy Fuels* **2019**, *3* (11), 3116–3127.
- (8) Shi, M.; Song, C.; Tai, Z.; Zou, K.; Duan, Y.; Dai, X.; Sun, J.; Chen, Y.; Liu, Y. Coal-Derived Synthetic Graphite with High Specific Capacity and Excellent Cyclic Stability as Anode Material for Lithium-Ion Batteries. *Fuel* **2021**, *292*, 120250.
- (9) Zhou, X.; Chen, F.; Bai, T.; Long, B.; Liao, Q.; Ren, Y.; Yang, J. Interconnected Highly Graphitic Carbon Nanosheets Derived from Wheat Stalk as High Performance Anode Materials for Lithium Ion Batteries. *Green Chem.* **2016**, *18* (7), 2078–2088.
- (10) Jurkiewicz, K.; Pawlyta, M.; Zygadlo, D.; Chrobak, D.; Duber, S.; Wrzalik, R.; Ratuszna, A.; Burian, A. Evolution of Glassy Carbon under Heat Treatment: Correlation Structure-Mechanical Properties. *J. Mater. Sci.* **2018**, *53* (5), 3509–3523.
- (11) Pei, X.; Shen, B.; Zhang, L.; Zhai, W.; Zheng, W. Accelerating the Graphitization Process of Polyimide by Addition of Graphene. *J. Appl. Polym. Sci.* **2015**, *132* (2), 41274.
- (12) Oya, A.; Otani, S. Influences of Particle Size of Metal on Catalytic Graphitization of Non-Graphitizing Carbons. *Carbon* **1981**, *19* (5), 391–400.
- (13) Jiang, X.; Chen, Y.; Meng, X.; Cao, W.; Liu, C.; Huang, Q.; Naik, N.; Murugadoss, V.; Huang, M.; Guo, Z. The Impact of Electrode with Carbon Materials on Safety Performance of Lithium-Ion Batteries: A Review. *Carbon* **2022**, *191*, 448–470.
- (14) Sundqvist, B. Carbon Under Pressure. *Phys. Rep.* **2021**, *909*, 1–73.
- (15) Vieira, L. d. S. A Review on the Use of Glassy Carbon in Advanced Technological Applications. *Carbon* **2022**, *186*, 282–302.
- (16) Hu, M.; Zhang, S.; Liu, B.; Wu, Y.; Luo, K.; Li, Z.; Ma, M.; Yu, D.; Liu, L.; Gao, Y.; Zhao, Z.; Kono, Y.; Bai, L.; Shen, G.; Hu, W.; Zhang, Y.; Riedel, R.; Xu, B.; He, J.; Tian, Y. Heat-Treated Glassy Carbon under Pressure Exhibiting Superior Hardness, Strength and Elasticity. *J. Mater.* **2021**, *7*, 177–184.
- (17) Silverman, A.; Adler, J.; Kalish, R. Diamond Membrane Surface after Ion-Implantation-Induced Graphitization for Graphite Removal: Molecular Dynamics Simulation. *Phys. Rev. B: Condens. Matter Mater. Phys.* **2011**, *83*, 224206.
- (18) Liu, B.; Zhao, H.; Li, X.; Yang, Z.; Zhang, D.; Liu, Z. Effect of Pore Structure on the Thermophysical and Frictional Properties of High-Density Graphite. *Microporous Mesoporous Mater.* **2022**, *330*, 111613.
- (19) Zhang, L.; Kowalik, M.; Mao, Q.; Damirchi, B.; Zhang, Y.; Bradford, P. D.; Li, Q.; van Duin, A. C. T.; Zhu, Y. T. Joint Theoretical and Experimental Study of Stress Graphitization in Aligned Carbon Nanotube/Carbon Matrix Composites. *ACS Appl. Mater. Interfaces* **2023**, *15* (27), 32656–32666.
- (20) Savage, G. The Properties of Carbon-Carbon Composites. *Carbon-Carbon Composites*; Springer Netherlands: Dordrecht, 1993; pp 277–322.
- (21) Yan, Z.; Huang, D.; Lai, A.; Chu, Y.; Zheng, F.; Cai, Y.; Pan, Q.; Wang, H.; Huang, Y.; Li, Q. Nickel Catalyzed Graphitized Carbon Coated  $\text{LiFe}_{1-x}\text{Ni}_x\text{PO}_4$  Composites as Cathode Material for High-Performance Lithium-Ion Batteries. *Electrochim. Acta* **2020**, *353* (1), 136565.
- (22) Choi, B.-K.; Choi, W.-K.; Seo, M.-K. Effect of Catalytic Graphitization on the Electric Heating Performance of Electroless Nickel-Coated Carbon Fibers. *Curr. Appl. Phys.* **2022**, *42*, 86–91.
- (23) Li, H.; Zhang, H.; Li, K.; Zhang, J.; Sun, M.; Su, B. Catalytic Graphitization of Coke carbon by iron: Understanding the Evolution of Carbon Structure, Morphology and Lattice Fringes. *Fuel* **2020**, *279* (1), 118531.
- (24) Destyorini, F.; Yudianti, R.; Irmawati, Y.; Hardiansyah, A.; Hsu, Y.-I.; Uyama, H. Temperature Driven Structural Transition in the Nickel-based Catalytic Graphitization of Coconut Coir. *Diamond Relat. Mater.* **2021**, *117*, 108443.
- (25) Hunter, R. D.; Ramírez-Rico, J.; Schnepf, Z. Iron-Catalyzed Graphitization for the Synthesis of Nanostructured Graphitic Carbons. *J. Mater. Chem. A* **2022**, *10*, 4489–4516.
- (26) Zhou, H.; Yu, Q.; Peng, Q.; Wang, H.; Chen, J.; Kuang, Y. Catalytic Graphitization of Carbon Fibers with Electrodeposited Ni-B Alloy Coating. *Mater. Chem. Phys.* **2008**, *110* (2–3), 434–439.
- (27) Tzeng, S. S. Catalytic Graphitization of Electroless Ni-P Coated PAN-Based Carbon Fibers. *Carbon* **2006**, *44* (10), 1986–1993.
- (28) Yoshimura, S.; Chang, R. P. H. *Supercarbon: Synthesis, Properties and Applications*; Springer-Verlag: New York, 1998.
- (29) Zhu, X.; Liu, M.; Qi, X.; Li, H.; Zhang, Y. F.; Li, Z.; Peng, Z.; Yang, J.; Qian, L.; Xu, Q.; Gou, N.; He, J.; Li, D.; Lan, H. Templateless, Plating-Free Fabrication of Flexible Transparent Electrodes with Embedded Silver Mesh by Electric-Field-Driven Microscale 3D Printing and Hybrid Hot Embossing. *Adv. Mater.* **2021**, *33*, 2007772.
- (30) Loto, C. A. Electroless Nickel Plating - A Review. *Silicon* **2016**, *8*, 177–186.
- (31) Vitry, V.; Hastir, J.; Megret, A.; Yazdani, S.; Yunacti, M.; Bonin, L. Recent Advances in Electroless Nickel-Boron coatings. *Surf. Coat. Technol.* **2022**, *429*, 127937.
- (32) Nazari, H.; Barati Darband, G.; Arefinia, R. A Review on Electroless Ni-P Nanocomposite Coatings: Effect of Hard, Soft, and Synergistic Nanoparticles. *J. Mater. Sci.* **2023**, *58*, 4292–4358.

- (33) Shozib, I. A.; Ahmad, A.; Abdul-Rani, A.; Beheshti, M.; Aliyu, A. A Review on the Corrosion Resistance of Electroless Ni-P based Composite Coatings and Electrochemical Corrosion Testing Methods. *Corros. Rev.* **2022**, *40* (1), 1–37.
- (34) Uchiyama, H.; Sone, M.; Ishiyama, C.; Endo, T.; Hatsuzawa, T.; Higo, Y. Uniform Ni-P Film Using an Electroless Plating Method with an Emulsion of Supercritical Carbon Dioxide. *J. Electrochem. Soc.* **2007**, *154* (7), No. E91.
- (35) Huang, Z.; Nguyen, T. T.; Zhou, Y.; Qi, G. A Low Temperature Electroless Nickel Plating Chemistry. *Surf. Coat. Technol.* **2019**, *372*, 160–165.
- (36) Sudagar, J.; Lian, J.; Sha, W. Electroless Nickel Alloy, Composite and Nano Coatings - A Critical Review. *J. Alloys Compd.* **2013**, *571*, 183–204.
- (37) Yun, S.; Ted Oyama, S. Correlations in palladium membranes for hydrogen separation: A review. *J. Membr. Sci.* **2011**, *375* (1–2), 28–45.
- (38) Thakur, A.; Gharde, S.; Kandasubramanian, B. Electroless Nickel Fabrication on Surface Modified Magnesium Substrates. *Def. Technol.* **2019**, *15* (4), 636–644.
- (39) Zhang, H.; Lu, Y.; Gu, C.-D.; Wang, X.-L.; Tu, J.-P. Ionothermal Synthesis and Lithium Storage Performance of Core/Shell Structured Amorphous@Crystalline Ni-P Nanoparticles. *CrytEngComm* **2012**, *14*, 7942–7950.
- (40) Li, Z.; Bian, C.; Hu, L. Exploration of the Corrosion Behavior of Electroless Plated Ni-P Amorphous Alloys via X-ray Photoelectron Spectroscopy. *Molecules* **2023**, *28*, 377.
- (41) Barnakov, C. N.; Khokhlova, G. P.; Popova, A. N.; Sozinov, S. A.; Ismagilov, Z. R. XRD Characterization of the Structure of Graphites and Carbon Materials Obtained by the Low-Temperature Graphitization of Coal Tar Pitch. *Eurasian Chem.-Technol. J.* **2015**, *17* (2), 87–93.
- (42) Atria, J. V.; Rusinko, F.; Schobert, H. H. Structural Ordering of Pennsylvania Anthracites on Heat Treatment to 2000–2900 °C. *Energy Fuels* **2002**, *16* (6), 1343–1347.
- (43) Pimenta, M. A.; Dresselhaus, G.; Dresselhaus, M. S.; Cançado, L. G.; Jorio, A.; Saito, R. Studying Disorder in Graphite-Based Systems by Raman Spectroscopy. *Phys. Chem. Chem. Phys.* **2007**, *9*, 1276–1290.
- (44) Sadezky, A.; Muckenhuber, H.; Grothe, H.; Niessner, R.; Pöschl, U. Raman Microspectroscopy of Soot and Related Carbonaceous Materials: Spectral Analysis and Structural Information. *Carbon* **2005**, *43* (8), 1731–1742.
- (45) Kumar, A.; Patil, S.; Joshi, A.; Bhoraskar, V.; Datar, S.; Alegaonkar, P. Mixed Phase,  $sp^2$ - $sp^3$  Bonded, and Disordered Few Layer Graphene-like Nanocarbon: Synthesis and Characterizations. *Appl. Surf. Sci.* **2013**, *271*, 86–92.
- (46) Choi, G. B.; Hong, S.; Wee, J. H.; Kim, D. W.; Seo, T. H.; Nomura, K.; Nishihara, H.; Kim, Y. A. Quantifying Carbon Edge Sites on Depressing Hydrogen Evolution Reaction Activity. *Nano Lett.* **2020**, *20* (8), 5885–5892.
- (47) Wang, J.; Morishita, K.; Takarada, T. High-Temperature Interactions between Coal Char and Mixtures of Calcium Oxide, Quartz, and Kaolinite. *Energy Fuels* **2001**, *15* (5), 1145–1152.
- (48) Roy, A.; Srinivas, V.; Ram, S.; De Toro, J. A.; Mizutani, U. Structure and Magnetic Properties of Oxygen-Stabilized Tetragonal Ni Nanoparticles Prepared by Borohydride Reduction Method. *Phys. Rev. B: Condens. Matter Mater. Phys.* **2005**, *71*, 184443.
- (49) Zhang, J.; Liu, H.; Shi, P.; Li, Y.; Huang, L.; Mai, W.; Tan, S.; Cai, X. Growth of Nickel (111) Plane: The Key Role in Nickel for Further Improving the Electrochemical Property of Hexagonal Nickel Hydroxide-Nickel & Reduced Graphene Oxide Composite. *J. Power Sources* **2014**, *267*, 356–365.
- (50) Tang, X.; Gao, S.; Zhang, D.; Xia, X.; Wang, J.; She, W.; Yang, B.; Meng, X.; Wang, K.; Han, Z.; Wang, B. One-Step Solid-State Synthesis of  $Ni_xP_y$ @C Nanocomposites for High-Performance Hybrid Supercapacitor. *J. Alloys Compd.* **2022**, *923*, 166289.
- (51) Lu, D.; Yuan, F.; Ni, Y.; Wan, M.; Cheng, X. Phase-Control Synthesis and Catalytic Property of Magnetic  $Ni@Ni_xP_y$  Core-Shell Microstructures. *Mater. Res. Bull.* **2018**, *101*, 215–222.
- (52) Raupp', G. B.; Delgass, W. N. Mössbauer investigation of supported Fe and FeNi catalysts II. Carbides formed Fischer-Tropsch synthesis. *J. Catal.* **1979**, *58* (3), 348–360.
- (53) Fernandes, C. M.; Senos, A. M. R. Cemented Carbide Phase Diagrams: A Review. *Int. J. Refract. Met. Hard Mater.* **2011**, *29*, 405–418.